Utilizing internal resonant scattering to improve photoluminescence energy outcoupling of CsPbBr3/Cs4PbBr6 perovskite phosphor

Zong-Tao Li, Bo-Jia Li, Jia-Sheng Li, Cun-Jiang Song, Xin-Rui Ding, Hai-Long Yuan, Bin-Hai Yu, Yong Tang, Jian-Zhen Ou, Romain Gautier, et al.

▶ **To cite this version:**

Zong-Tao Li, Bo-Jia Li, Jia-Sheng Li, Cun-Jiang Song, Xin-Rui Ding, et al.. Utilizing internal resonant scattering to improve photoluminescence energy outcoupling of CsPbBr3/Cs4PbBr6 perovskite phosphor. Chemical Engineering Journal, 2023, 476, pp.146457. 10.1016/j.cej.2023.146457 . hal-04273729

HAL Id: hal-04273729
https://hal.science/hal-04273729v1

Submitted on 7 Nov 2023

HAL is a multi-disciplinary open access archive for the deposit and dissemination of scientific research documents, whether they are published or not. The documents may come from teaching and research institutions in France or abroad, or from public or private research centers.

L'archive ouverte pluridisciplinaire **HAL**, est destinée au dépôt et à la diffusion de documents scientifiques de niveau recherche, publiés ou non, émanant des établissements d'enseignement et de recherche français ou étrangers, des laboratoires publics ou privés.

Utilizing Internal Resonant Scattering to Improve Photoluminescence Energy Outcoupling of $CsPbBr_3/Cs_4PbBr_6$ Perovskite Phosphor

Zong-Tao Li[a,b], Bo-Jia Li[a], Jia-Sheng Li[a,*], Cun-Jiang Song[a], Xin-Rui Ding[a], Hai-Long Yuan[a,b], Bin-Hai Yu[a], Yong Tang[a], Jian-Zhen Ou[c], Romain Gautier[d], Hong-Lei Ji[e], Hao-Chung Kuo[f]

[a]*National & Local Joint Engineering Research Center of Semiconductor Display and Optical Communication Devices, South China University of Technology, Guangzhou 510641, China*

[b]*Guangdong Provincial Key Laboratory of Semiconductor Micro Display, Foshan Nationstar Optoelectronics Company Ltd., Foshan 528000, China*

[c]*School of Engineering, RMIT University Melbourne, Victoria 3000, Australia*

[d]*Institut des Matériaux Jean Rouxel, Université de Nantes, CNRS, 2 rue de la Houssinière B.P. 32229, 44322 Nantes cedex 3, France*

[e]*R & D Center, TCL Electronics Holdings Limited, Shenzhen 518052, China*

[f]*Department of Photonics and Institute of Electro-Optical Engineering, College of Electrical and Computer Engineering, National Chiao Tung University, Hsinchu 30010, Taiwan, China*

**Corresponding author. Email:* jiasli@scut.edu.cn

Abstract

Although stable perovskite phosphors, i.e., $CsPbBr_3/Cs_4PbBr_6$, were extensively reported and made great progress, achieving strong photoluminescence (PL) energy outcoupling remains challenging owing to their short Stoke's shift with serious PL energy absorption. This study utilized internal resonant scattering (IRS) to improve the PL energy outcoupling (PEO) of $CsPbBr_3/Cs_4PbBr_6$ perovskite phosphor, which was realized by the nanopore-packing perovskite particles (NP-PPs) structure inside a phosphor. The nano-porous matrix hybrid solid-liquid interfacial reaction was developed to construct NP-PPs in a phosphor, and it is optimized to achieve a denser NP-PP structure with an enhanced PEO effect (2.8-fold enhanced PL intensity). Numerical results revealed that the NP-PP structure transforms the PL energy absorption mode to the IRS mode, most of the scattering PL energy evades NP-PPs instead of propagating inside. The optimized phosphor was applied to white devices, and we finally achieved an ultrahigh luminous efficacy of 131.32 lm/W based on green perovskite phosphors. This study provides a general guide for efficient perovskite phosphors utilizing the nano-porous matrix to enable the IRS effect.

Keywords: $CsPbBr_3/Cs_4PbBr_6$ perovskite; light-emitting diode; photoluminescence energy outcoupling; internal resonant scattering; efficiency

1. Introduction

Perovskite phosphors are promising as color converters in optoelectronic devices, *i.e.*, light-emitting diodes (LEDs), because of their narrow band emission, wide tunable bandgap, and high defect tolerance [1-7]. Since Kovalenko's group first synthesize the nanocrystals of cesium lead halide perovskite $CsPbX_3$ [8], great efforts have focused on improving the photoluminescence quantum yield (PLQY) of perovskites phosphor. Nowadays, their PLQYs generally range from 85%-100% [9, 10], which is as high as mature phosphor materials including the yttrium aluminum garnet:Ce phosphor, β-Sialon:Eu^{2+} phosphor, CdSe phosphor, and so on [11, 12]. Recently, Zhong et al. indicated that the lifespan of perovskite color converters has been largely improved to meet industry standards [13]. Especially, green composite perovskite phosphors composed of two or more halide perovskite phases (Cs_4PbBr_6 and $CsPbBr_3$, $CsPb_2Br_5$ and $CsPbBr_3$, etc.) perform remarkable stability in perovskite phosphors, as the $CsPbBr_3$ emitters are well passivated by Cs_4PbBr_6 or $CsPb_2Br_5$ [14, 15], and thereby demonstrating a superior durable high-power-driving capability at an ultrahigh working current of 300 mA [16]. Additionally, perovskite phosphors are necessary to achieve high PL intensity to satisfy the luminous efficacy (LE) requirement of wide-color-gamut white LEDs, which needs to advance toward the practical limit of 250 lm/W by 2035 [17]. Unfortunately, the PL intensity enhancement is limited by the low PL energy outcoupling (PEO) of perovskite phosphors, leading to the disappointing LE of white LEDs (generally < 90 lm/W [18, 19]), although they

have great PLQY compared with mature rare-earth and CdSe phosphors (> 200 lm/W) [20]. Therefore, improving the PEO is necessary and challenging, which becomes a bottleneck for the application of perovskite phosphors in efficient wide-color gamut white devices [21-23].

The low PEO of perovskite phosphors is generally attributed to the short Stokes' shift [24], the PL energy emitting from a perovskite phosphor is easily absorbed by perovskite phosphors themselves, especially when the device have a high optical density of perovskite phosphors [25]. What is worse, the high surface energy of perovskite particles leads to easy aggregation. The aggregated large-size particle has a long light path of PL photons and leads to a so-called aggregation-induced PL energy absorption [26, 27]. Therefore, previous studies mainly focused on reducing the aggregation of perovskite particles for the PEO improvement. For examples, dispersing matrices (e.g., nanocelluloses [28], polymer frameworks [29], diatomite [30], silica spheres [31, 32] and metal-organic frameworks [33-35]) are widely utilized to suppress the aggregation of perovskite particles through physical or chemical integration. As for a less-aggregated discrete perovskite particle (DPP) with smaller size and shorter optical path, the PL energy suffers from a lower absorption before escaping to the matrix [36]. As for a multiple perovskite particles (MPP) system, the escaping PL energy further suffers from serious absorption by a great amount of other perovskite particles in the matrix [25], and the PEO mechanism is still unclear. Especially,

previous studies almost concentrated on naturally unstable single-phase perovskite phosphors, the dispersing matrices are also well designed to ensure the high stability of perovskite phosphors, such as introducing dense ligands [37, 38], protective layers [23, 34], and so on, which further aggravates the PL energy absorption. As mentioned above, the $CsPbBr_3/Cs_4PbBr_6$ perovskite phosphor is with high stability, as well as its simple structure mainly occupied by the Cs_4PbBr_6 without ligand modification, showing great potential to achieve high PEO, while its *in-situ* synthesis in a dispersing matrix and the PEO enhanced mechanism are barely concerned.

In this study, we utilized internal resonant scattering (IRS) to improve the PEO of $CsPbBr_3/Cs_4PbBr_6$ perovskite phosphor, which was realized by the nanopore-packing perovskite particles (NP-PPs) inside a phosphor. A nano-porous matrix hybrid solid-liquid interfacial (NMHS-LI) reaction was developed to prepare the NP-PP phosphor, and the key parameters including ultrasonic power and matrix content were optimized to achieve the NP-PP phosphor with improved PL intensity. A finite-difference time-domain (FDTD) model was introduced to confirm the enhanced PEO of NP-PP phosphor, demonstrating an IRS effect to suppress the PL energy absorption for the MPP system. The optimized phosphor was finally applied to the white LEDs, achieving an ultrahigh LE of 131.32 lm/W based on green perovskite phosphors, which is much higher than that in common reports. This strategy provides a general guide for highly

efficient and stable perovskite phosphors utilizing nano-porous matrices.

2. Results and discussion

2.1 NP-PP Phosphor Preparation

Herein, a hydrophobic SiO_2-aerogel was selected as a nano-porous matrix to construct the NP-PP structure in a $CsPbBr_3/Cs_4PbBr_6$ perovskite phosphor. Reasons are as follows:1) its open porous network with moderate nanopores (20-80 nm) is helpful for the solid precursor fully integration with the matrix; 2) such a size range of nanopores is helpful to avoid the PL energy absorption in a perovskite particle, and its low refractive index for visible light is enough to enable the IRS effect, which will be discussed at the subsequence numerical study; 3) its hydrophobic nanorough surface can avoid the large aggregation among NP-PP phosphors, and also help to resist water and oxygen erosion. Accordingly, we developed a NMHS-LI reaction method to preparing the NP-PP phosphor, as shown in **Fig. 1**. Firstly, the SiO_2-aerogel/CsBr hybrid solid precursor was prepared for subsequent reaction. The hydrophobic aerogel was uniformly dispersed into an ethanol solvent, and then mixed with hydrophilic CsBr in water (**Fig. S1**). After the facile wet-mixing and evaporation process, a hybrid solid precursor with CsBr particles embedded in the aerogel matrix was obtained (**Fig. S2**) owing to the recrystallization of CsBr particles inside the nanopores of the aerogel. Next, after grinding, excessive hybrid solid precursors were added to the liquid precursor of $PbBr_2$ in DMF solvent. Herein, we utilized the efficient ultrasonication to provide reaction energy for the solid-liquid interface reaction

instead of heating as previous study [39], as the ultrasonication can largely reduce the process time (less than half an hour) and improved the dispersity of particles. During the NMHS-LI reaction, the $PbBr_2$ precursors were dissolved in DMF; the SiO_2-aerogel/CsBr hybrid precursors were just broken with their aerogel matrix structure kept, owing to the insolubility of CsBr and SiO_2 in DMF. Additionally, the matrix structure provided numerous reaction sites for perovskite synthesis. Therefore, these conditions enabled the Pb^{2+} ions to *in-situ* synthesize NP-PP phosphor on the matrix with the hybrid precursors. The Pb:Cs ratio was optimized to 1:6 for achieving the maximum PLQY (38.6%) of $CsPbBr_3/Cs_4PbBr_6$ phosphor without dispersing matrix, which was also used as the controlled group (called as pure perovskite phosphors), and details of which can be found in **Fig. S3**. During the NMHS-LI reaction, the hybrid solids at the bottom of the DMF solvent changed from orange to yellow-green (**Fig. S4**), indicating that the NP-PP phosphor was synthesized. As our NP-PP phosphor was entirely ligand-free, the ligand shedding was out of consideration [40], and the product can be transferred to a highly volatile organic solvent (n-hexane) for rapid drying within several minutes, and then easily achieving the solid-state NP-PP phosphor.

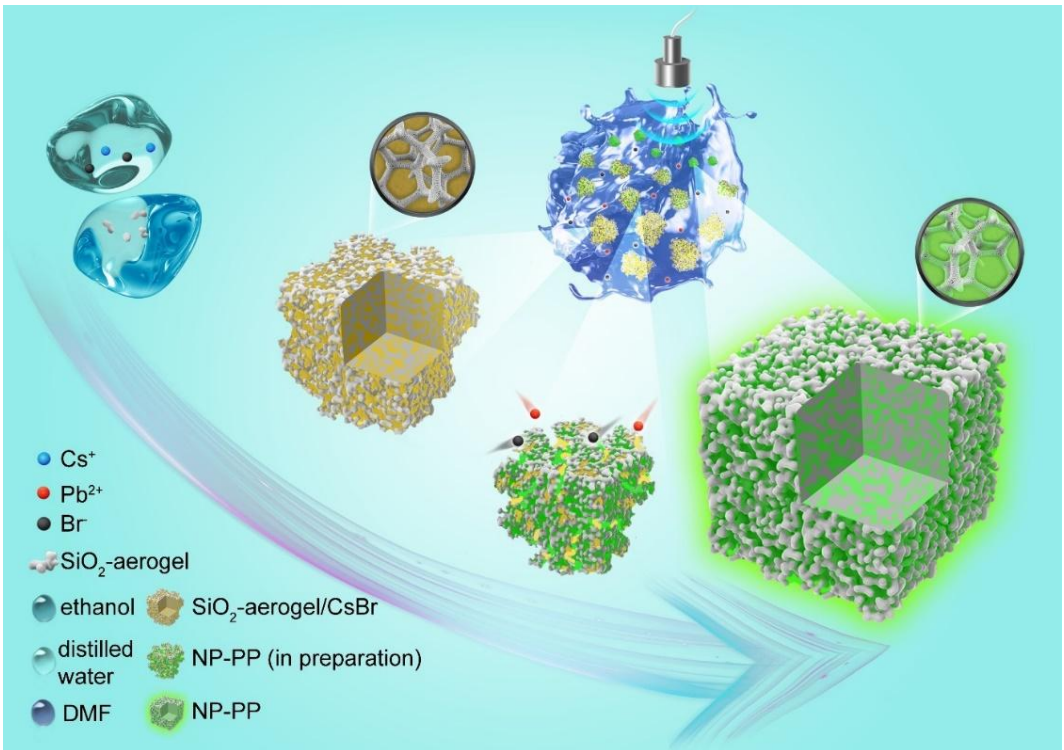

Fig. 1. In-situ synthesis process of NP-PP phosphor via the NMHS-LI reaction.

To confirm the successful synthesis of the NP-PP phosphor, its scanning electron microscopy (SEM) morphology was analyzed, as shown in **Fig. 2**. The ultrasonic power and matrix content were maintained at 40 W and 3.5 wt%, respectively; these two key factors will be discussed in detail subsequently. **Fig. 2a-f** show the morphology of NP-PP phosphor and its elemental mapping. The Si originates from the aerogel matrix, whereas the Cs, Pb, and Br are from perovskite nanocrystals. These elements overlap greatly, demonstrating a uniform NMHS-LI reaction in the NP-PP phosphor. To confirm the uniform distribution of NP-PPs in

the internal region of the aerogel matrix, elemental mappings of the cross-sectional phosphor were obtained using focused ion beam (FIB) cutting (**Fig. S5**). And the high-resolution Transmission electron microscope (TEM) images also verify that the perovskite nanocrystals were synthesized in the matrix (**Fig. S6**). Additionally, the surface and cross-sectional morphologies of the NP-PP phosphor were investigated, as shown in **Fig. 2g** and **Fig. S7**, respectively. This phosphor presented a nanorough surface, originating from the nano-porous structure of the aerogel matrix, which can be further supported by the smooth surface of the pure perovskite phosphor without an aerogel matrix *in-situ* encapsulant (**Fig. S8**).

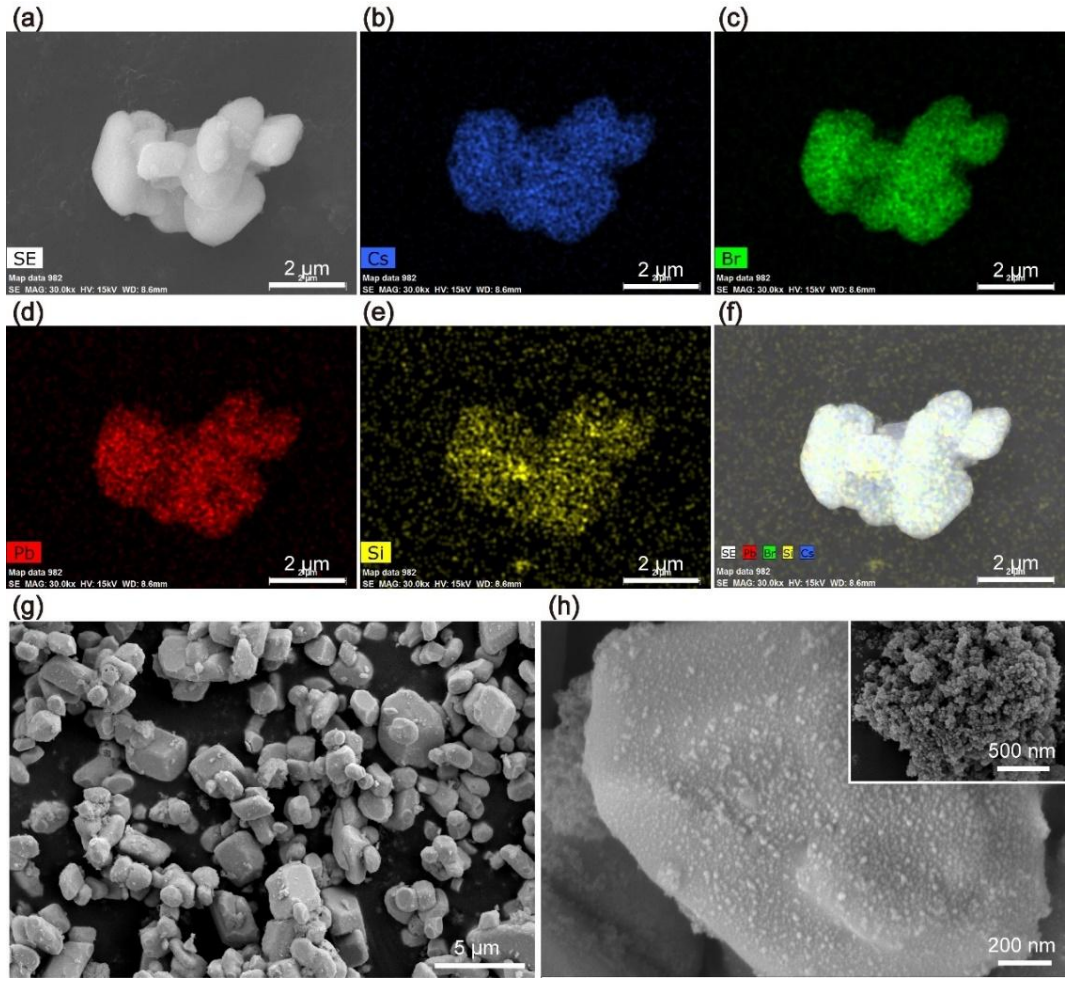

Fig. 2. Morphology of NP-PP phosphor. (a) SEM image of NP-PP phosphor for element mapping. (b)-(f) Element mappings of Si, Cs, Br, Pb, and their composites, respectively. (g)-(h) SEM images of NP-PP phosphor at a different magnification. Inset: SEM image of an aerogel matrix.

2.2 Structure Optimization of NP-PP phosphor

2.2.1 Morphology and dispersity

The NP-PP structure was ensured to be well *in-situ* synthesized inside the

phosphor by optimizing the ultrasonic power and matrix content, which are two key factors of the NMHS-LI reaction process. For the first key parameter, external energy provides activation energy for the chemical reaction [39]; and the ultrasonic power breaks up both the precursor particles and aggregated particles, which refines the products and accelerates the synthesis [41, 42]. Therefore, the ultrasonic power has great impacts on the NMHS-LI. For the second key parameter, the SiO_2-aerogel matrix provides its nano porous structure for the NP-PP phosphor. The higher the matrix content, the denser the NP-PP structure, which significantly affects their optical properties. Above two impacts will be discussed later. The SEM morphologies of the NP-PP phosphor at different ultrasonic powers are shown in **Fig. 3a-d**. We found that NP-PP phosphor particles without ultrasonication were smaller than that of the hybrid solid precursors of SiO_2-aerogel/CsBr. This means that the supersaturated hybrid solid precursors were locally broken in NMHS-LI reaction to crystalized into perovskite crystals. Moreover, the particle size of the NP-PP phosphor decreased as the ultrasonic power increased from 0 to 40 W, with a reduction in mean particle size from 2.7 to 1.7 μm (**Fig. S9**). To have a deep understand, the X-ray diffraction (XRD) patterns were provided in **Fig. 3e** for Qualitative analysis. We found that the enhanced ultrasonic power also helps accelerate the NMHS-LI reaction, which was exhibited by the decreased CsBr peak in the X-ray diffraction (XRD) patterns. Moreover, the XRD patterns (CsBr and Cs_4PbBr_6 peaks) of the phosphor were almost unchanged after the ultrasonic power reached 30 W,

demonstrating that the NMHS-LI reaction of constructing NP-PPs was nearly complete. These results indicate that the synthetic NP-PP phosphor has good rigidity and is difficult to further dissociate by ultrasonication, and the dissociation of hybrid solid precursors occurs during the reaction as shown in **Fig. 3f**. As a result, the dissociation and reaction of the hybrid solid precursors are competitive with enhanced ultrasonic power, leading to a larger phosphor size with an excess ultrasonic power of over 40 W (**Fig. S10**). Nevertheless, the suitable ultrasonic power (~40 W in our case) is helpful for achieving the complete NP-PP structure with a concentrated and small size distribution.

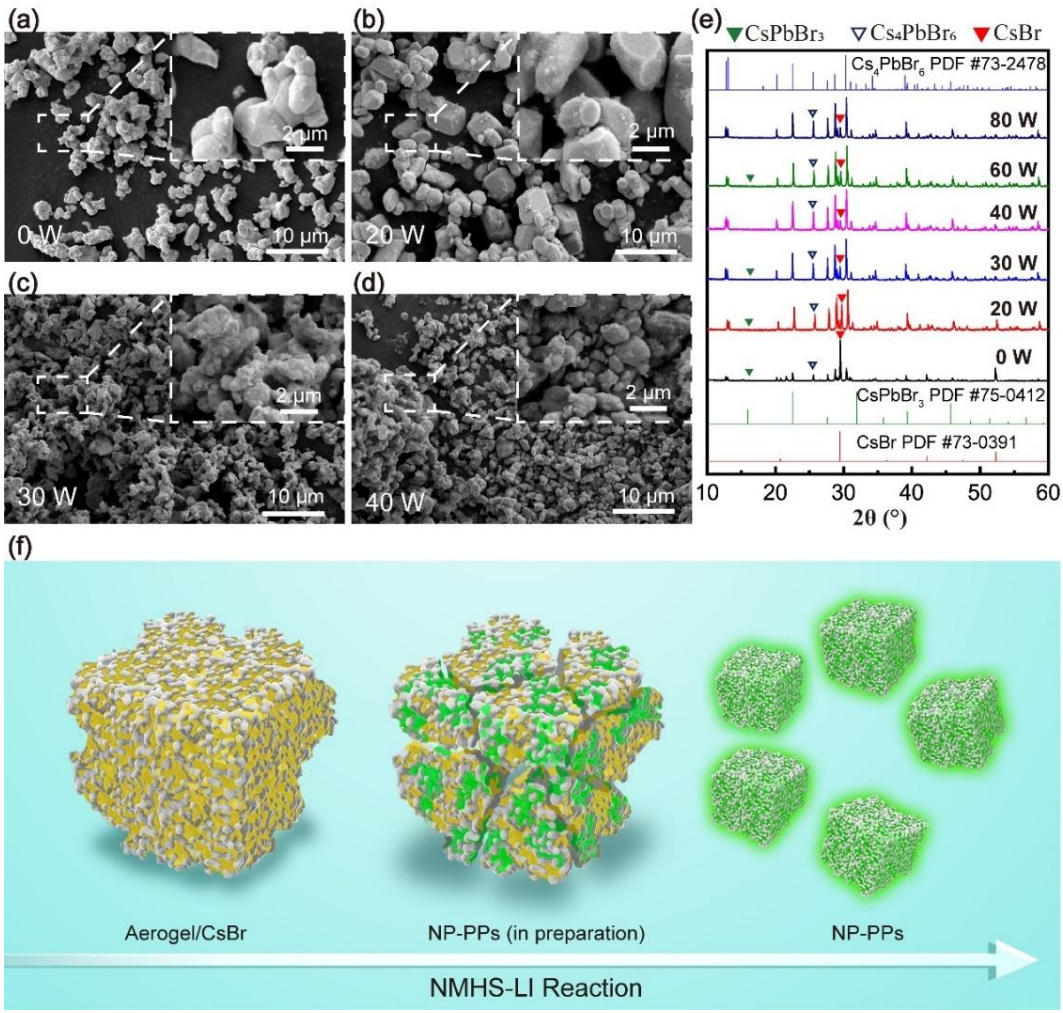

Fig. 3. Effect of ultrasonic power on the particle structure of NP-PP phosphor. (a)-(d) SEM morphology of NP-PP phosphor at ultrasonic powers of 0, 20, 30, and 40 W, respectively. (e) XRD patterns of NP-PP phosphor at different ultrasonic powers. (f) Diagram of dynamic processes of the seed dissociation and reaction under NMHS-LI reaction. The matrix content was 3.5 wt% for all samples.

The matrix content is the other key factor influencing the NP-PP structure, as shown in **Fig. 4a-d**. The pure perovskite phosphor without the aerogel matrix had a larger size than the NP-PP phosphor, indicating that the introduced matrix, with a large surface area for solvent interaction, was also beneficial to the dissociation of supersaturated hybrid solid precursors. Furthermore, we found that the phosphor size increased with an increase in matrix content; a larger size of 2 μm was observed as the matrix content increased to 5.7 wt% (**Fig. S11**). These results can also be explained by the accelerated reaction resulting from the increase in matrix content. Interestingly, the XRD peak of CsBr clearly decreased after introducing the matrix, as shown in **Fig. 4e**, indicating that the enhanced matrix content also helps to obtain the NP-PP structure. One possibility is that the nano porous structure of the SiO_2-aerogel/CsBr seed, with a larger surface area, provides many more reaction sites for the CsBr in hybrid solid precursors and $PbBr_2$ in liquid precursors compared with the pure CsBr solid. Therefore, the dissociation and reaction of hybrid solid precursors are also competitive with increasing matrix content, reaching the optimal NP-PP structure and minimum mean size of 1.4 μm at a matrix content of 3.5 wt%, which is smaller than that of the pure perovskite phosphor (mean size = 3.5 μm).

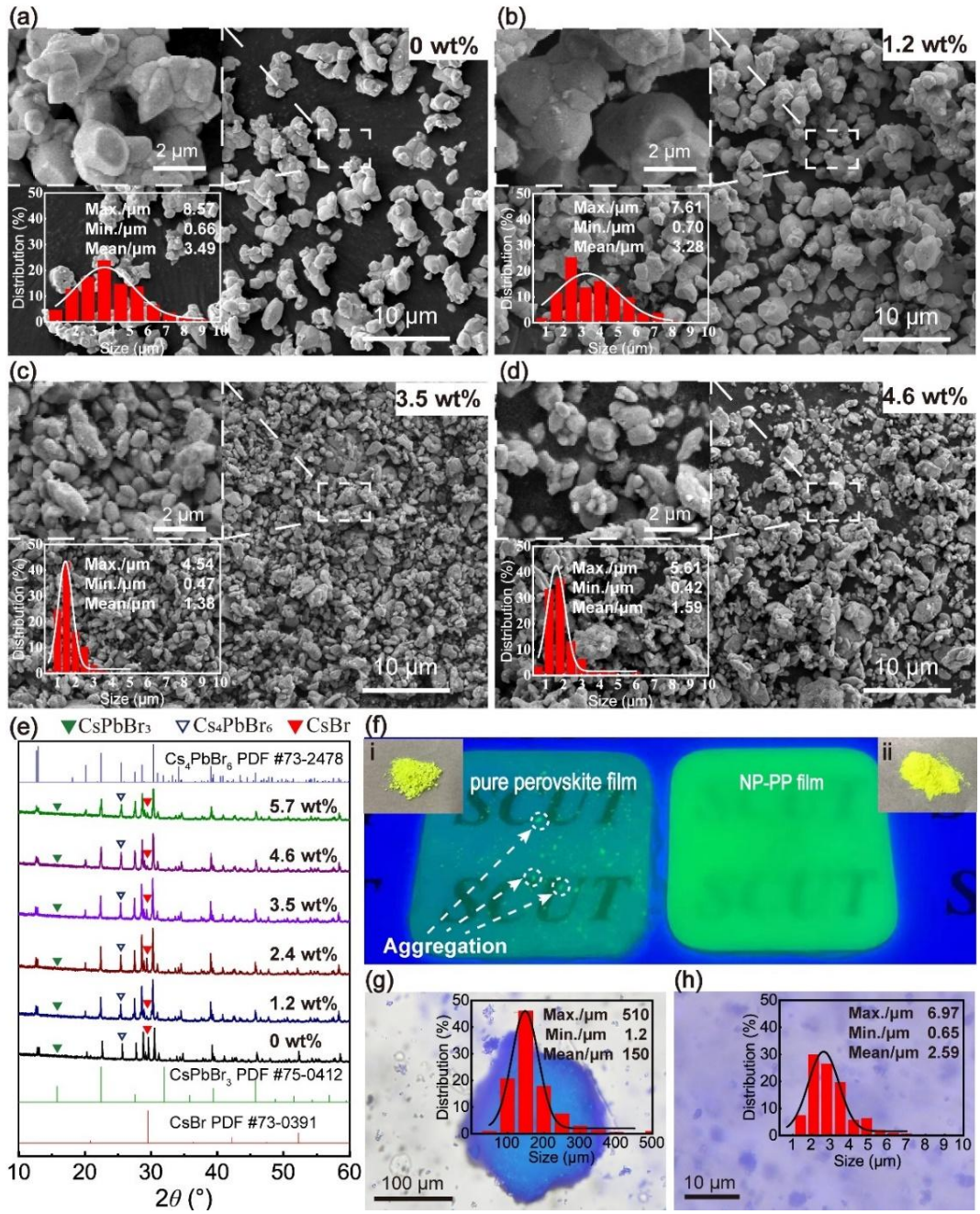

Fig. 4. Effect of matrix content on the particle structure of NP-PP phosphor. (a)-(d) SEM morphology of NP-PP phosphor with matrix contents of 0, 1.2, 3.5, and 4.6 wt%, respectively. The inserted cartograms show the corresponding

particle distribution. (e) XRD patterns of NP-PP phosphor with different matrix contents. (f) Photographs of pure perovskite and NP-PP films under UV irradiance, respectively. The insets are the images of (i) pure perovskite and (ii) NP-PP phosphors, respectively. (g-h) Particle size distributions of pure perovskite phosphor and NP-PP phosphor, respectively, after blending in silicone. The ultrasonic power for all samples was 40 W. The matrix content for NP-PP phosphors in films was 3.5 wt%. The phosphor concentration was 1.25 wt%.

In practice, the phosphor dispersity in packaging materials is much more essential than that in non-packaging ones because it mainly determines the application performance [43]. Herein, polydimethylsiloxane (PDMS) was selected as the packaging material to obtain phosphor films with good mechanical performance (**Fig. S12**). Photographs of the pure perovskite films and NP-PP films under UV light irradiation are shown in **Fig. 4f**; the latter exhibits almost no aggregation and a brighter green PL. To confirm the excellent dispersity of the NP-PP phosphor, the particle size distributions of the pure perovskite and NP-PP films were determined using confocal fluorescence images, as shown in **Fig. 4g**. Our optimized NP-PP phosphor after packaging, still had a small mean size of 2.6 μm with a size deviation of 1 μm, which is two orders of magnitude lower than that of the pure perovskite phosphor, which can be attributed to the hydrophobicity of the NP-PP structure as observed from the increase in contact angle from 0° to 130° (**Fig. S13**). Therefore, due to the hydrophobicity, the NP-PP

structure can also solve the aggregation issue as in previous studies, and the boosted PEO efficiency will be determined by the IRS effect as discussed later.

2.2.2 PLQY and PL intensity

The PLQY measurement was used to characterize the PL performance of the NP-PP phosphor before packaging, which is generally attributed to the crystal quality [6, 37]. According to the morphology investigation, the PLQY values of the NP-PP phosphor was also regulated by the ultrasonic power and matrix content, as shown in **Fig. 5a-b**, respectively. As for the ultrasonic power regulation, the PLQY reached a maximum value at the critical point of 40 W and then rolled off with excess ultrasonic power. One reasonable explanation is that the enhanced ultrasonic power mainly promotes the crystallization of the NP-PP phosphor before the complete reaction. However, it may introduce surface defects on NP-PPs because of the ultrasonic cavitation effect caused by excess reaction power, leading to more trap-assisted recombination. This notion is further supported by the increased slow-decay component a_2 in the PL decay measurement [44, 45], as the ultrasonic power exceeded 40 W (**Fig. S14** and **Table S1**). As for the matrix content regulation, the PLQY reached a maximum of 62% at the critical point of ~3.5 wt% (optimized NP-PP phosphor), significantly increasing by 55% compared with the pure perovskite phosphor without the matrix (PLQY of 40%). These results demonstrated that the matrix well passivated the surface defects of NP-PPs, which is consistent with previous reports using an SiO_2 shell as the

passivation layer for perovskites [46]. This notion is also supported by the longer PL decay lifetime of the NP-PP phosphor as the matrix content increased to 3.5 wt% (**Fig. S15** and **Table S2**) because the aerogel matrix introduces other recombination paths and led to a longer relaxation process. However, the PLQY rolled off with excess matrix, with a high matrix content of 5.7 wt% leading to a low PLQY. These results are further supported by the reduced PL decay lifetime with an excess matrix content of 5.7 wt%; in other words, fast and non-radiative recombination is introduced by an excess matrix content. The reason is that the CsBr content in hybrid solid precursors is insufficient for constructing continuous NP-PPs in the excess matrix, and a larger surface area is exposed without passivation, resulting in many more surface defects (more non-radiative recombination), as shown in **Fig. 5c**. Notably, achieving a high PLQY is out of the scope of our study, which can be further improved by optimizing crystal defects *via* ligand passivation in the future.

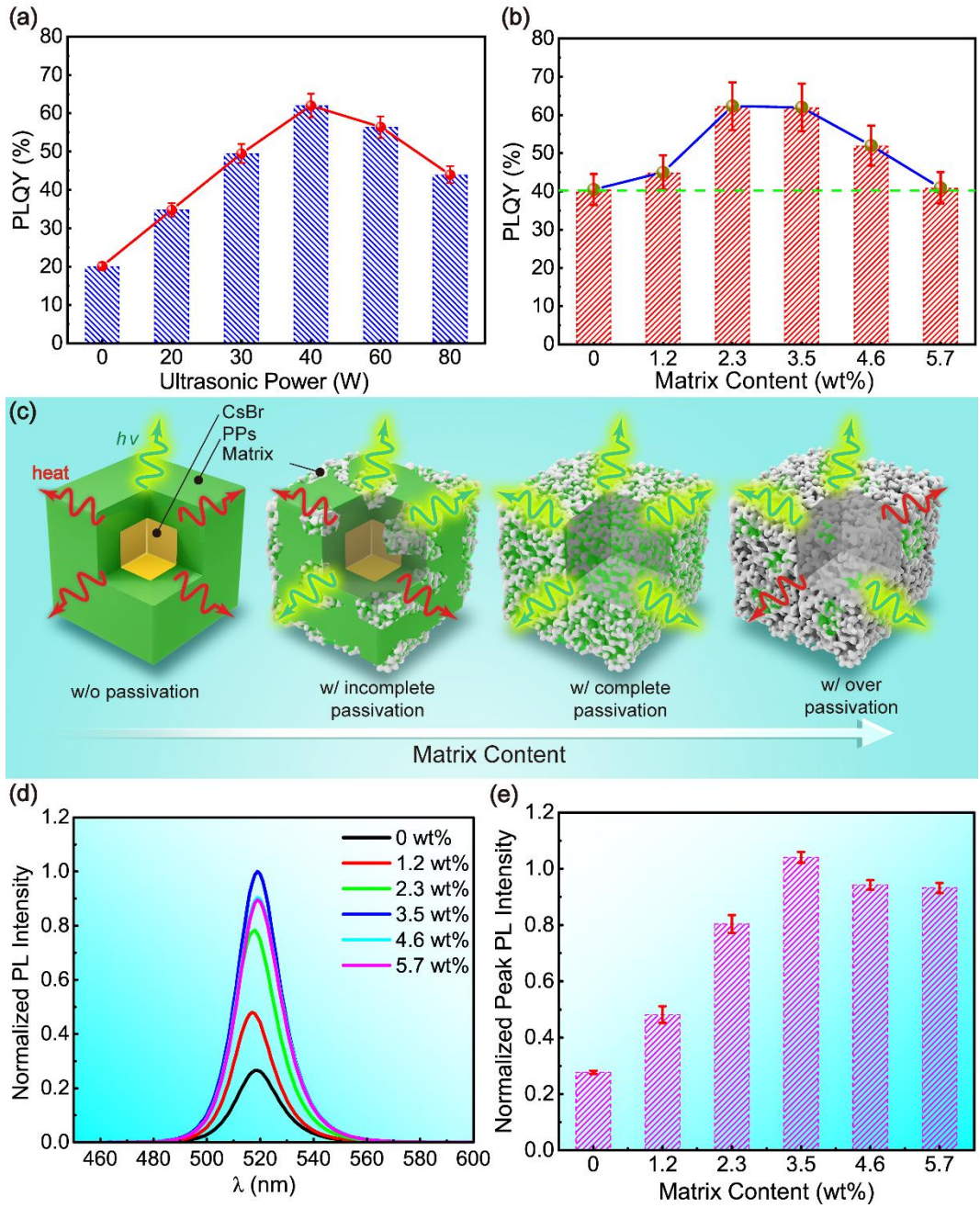

297

298 **Fig. 5. PL performance of NP-PP phosphor.** (a)-(b) PLQY of NP-PP phosphor
299 prepared at different ultrasonic powers (matrix content of 3.5 wt%) and matrix
300 contents (ultrasonic power of 40 W), respectively. (c) Diagram of NP-PP

phosphor with different matrix contents. (d) PL intensity and (e) peak PL intensity of NP-PP films with different matrix contents. The ultrasonic power was 40 W, and the phosphor concentration was 5 wt% for all samples.

In addition, the structure affects the light-matter interaction in the NP-PP phosphor. Particularly, although the phosphor size shows no significant difference as discussed in Section *2.2.1* (the aggregation difference is neglected), the increased matrix content leads to a higher density of NP-PP structures in the phosphor. The absorption and PL spectra of the NP-PP films (NP-PP phosphor packaging in silicone) with different matrix contents are shown in **Fig. S16** and **Fig. 5d**, respectively. The absorption spectra overlap with the PL spectrum around 520 nm due to the short Stoke's shift. The maximum PL intensity occurred at a matrix content of 3.5 wt%, the same as that of PLQY. For convenience, the peak PL intensity is shown in **Fig. 5e**. The peak PL intensity increased with the matrix content before reaching 3.5 wt% then decreased, whose trend is similar to that of PLQY. Interestingly, the optimized NP-PP films (matrix content of 3.5 wt%) show a boosted peak PL intensity 2.8-fold higher than that of the pure perovskite films. Therefore, the peak PL intensity largely benefited from the introduction of the aerogel matrix, especially at low matrix contents. However, at high matrix contents with a poor crystal quality as discussed above, the peak PL intensity only slightly declines. These results imply that a strong light-matter interaction exists in the perovskite phosphor with a denser NP-PP structure, which may originate

from the scattering effect of the aerogel matrix, as the haze of NP-PP films also increased with the matrix content (**Fig. S17**). FDTD simulations were subsequently carried out to investigate this issue and to confirm the PEO effect.

2.3 IRS effect of NP-PP phosphor

An FDTD simulation was performed to investigate the PL energy propagation of the NP-PP phosphor, revealing its PEO mechanisms. The FDTD simulation contained two cases: 1) PL energy propagating outward a DPP system, which characterizes the internal PL energy absorption in a perovskite particle; 2) PL energy propagating through a MPP system, which characterizes the overall PL energy absorption among perovskite particles. For the DPP system, the perovskite was assumed to be a cube, with its size varying from 5 nm to 10 μm (**Fig. S18**). For the MPP system, non-overlapping perovskite particles were assumed to be spherical uniformly and randomly distributed in a constant area, with their total volume invariable when their size varied (5 - 100 nm). Lastly, based on the MPP model, a NP-PP phosphor model was constructed, which was assumed to be an SiO_2 cube (400 nm) with random non-overlapping nanopores occupied by NP-PPs; the density and the size of NP-PPs were determined by the specific surface area (713 m^2/g), mean pore size (20 nm), and matrix content (from 0 to 6 wt%) used in our cases. Because the perovskite phosphor and NP-PP phosphor were mostly dominated by the Cs_4PbBr_6 component according to the XRD patterns, the effective refractive index of the perovskite particles was defined as 1.8 [47]. It is

difficult to directly characterize the dynamic color conversion in the FDTD method. Therefore, for the DPP system, a dipole source (520 nm) was located at the center of the perovskite particle for modeling the internal PL energy generation similar to previous reports [20, 22]. For the MPP system, a total-field scattered-field (TFSF) source (520 nm) closely surrounded the system for modeling the PL energy. The lower absorbance to the sources demonstrated better PEO effect.

For the DPP system, the absorbance of the perovskite particle significantly increased with a larger particle size, especially when the size reached the submicron scale (~100 nm) (**Fig. 6a**). These results are attributed to the serious absorption loss of PL energy inside the pure perovskite phosphor; a larger particle size leads to a longer internal absorption path and higher optical loss, which is consistent with previous reports [36, 48, 49]. Therefore, it is essential to control the size of NP-PPs below submicron scale, which further support our selection of aerogel with nanopores. As a result, we constructed a NP-PP structure in a perovskite phosphor using aerogel matrix. For the NP-PP phosphor with a MPP system, its absorbance with various matrix content is provided in **Fig. 6a**, the refractive index of matrix (MRI) is 1.5. The absorbance of the NP-PP phosphor decreases with the increased matrix content and well confirms the PEO enhancement of NP-PP structure; the absorbance fluctuates slightly when the matrix content over 3.5 wt%, which is consistent with the experimental results

achieving the maximum PL intensity.

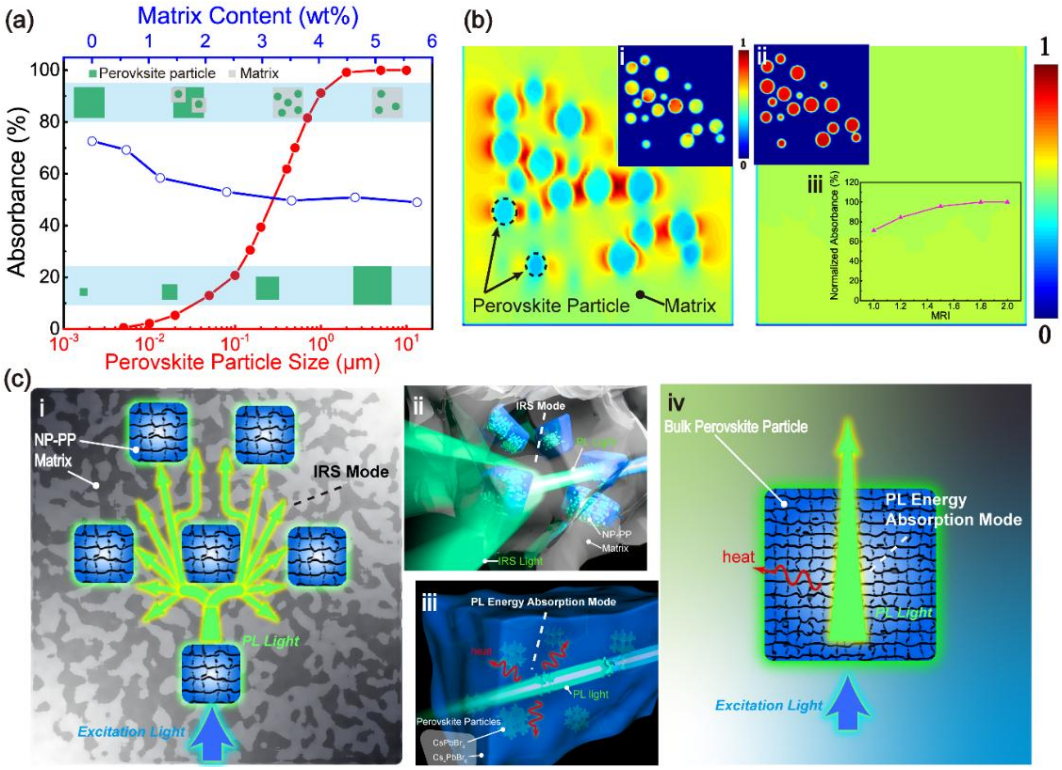

Fig. 6. PEO enhancement mechanism of NP-PP phosphor based on the IRS effect of the NP-PP structure. (a) Absorbance of the perovskite particle and NP-PP phosphor with different sizes and matrix contents, respectively. (b) Total-field and (i)-(ii) absorption-field energy flow density of the cross-sectional MPP system with its MRI of 1.0 (left) and 2.0 (right). Two color bars are normalized with all the total-field and absorption-field energy flow density, respectively. (iii) The normalized absorbance curve of the MPP system with different MRIs. (c) (i) PEO enhancement mechanisms through the IRS mode of the NP-PP structure compared to (iv) the PL energy absorption mode of a bulk perovskite particle. (ii)-(iii) 3D diagrams of (i) and (iv).

To have a deep understanding on the PEO enhancement, the energy flow densities of NP-PP phosphor in a MPP system were investigated as shown in **Fig. 6b**, and the NP-PP phosphor without aerogel matrix (MRI = 1.8) was as a reference. When the NP-PP phosphor had a low MRI, it was observed that the total-field energy flow density was lower inside the perovskite particles but dramatically higher near outside of the particle boundaries. One possibility is that the high refractive NP-PPs serve as the internal resonant scatters [50] in the MPP system, leading to the IRS effect. The strong scattering ability was further confirmed by its larger scattering cross-section (**Fig. S19**). These results mean that a portion of the PL energy is scattered when reaching NP-PPs, it tends to evade NP-PPs and propagating into the matrix; in other words, the PL energy absorption mode in NP-PPs transforms to the IRS mode in the matrix, as shown in **Fig. 6c**. The lower absorption-field energy flow density of NP-PPs with lower MRI can further support these results (**Fig. 6b-iii**), demonstrating the less PL energy absorption of NP-PPs in the aerogel matrix. In addition, the above IRS effect was also witnessed when changing the shape of NP-PPs (e.g., rectangle, ring, triangle) (**Fig. S20**), indicating that the IRS effect exists in nanoparticles of general shapes. Moreover, lower absorbance was obtained when a bulk perovskite particle (100 nm) was further divided into smaller particles, also supporting that the NP-PP structure could effectively suppresses the internal PL energy absorption of a bulk perovskite particle using the IRS effect (**Fig. S21**).

2.4 White LED applications of NP-PP phosphor

The NP-PP phosphor packaged in a blue LED chip confirmed the excellent PEO performance. Generally, the $CsPbBr_3$ color converter is used to compensate for the pure green spectra of LED devices, achieving white light for backlighting or pure green light for active display [2, 6, 51]. A high ratio of green light (RGL) from the color converter indicates excellent color tunability, particularly for mini/micro LED active display devices [52], which is determined by the PL intensity and can be obtained by increasing the phosphor concentration [53]. In our cases, the RGL is defined by the intensity ratio of the green spectra (495-565 nm) to the whole spectrum as shown in **Fig. 7a**. The RGL is enhanced as the phosphor concentration increases, which is consistent with previous reports [54]. However, the pure perovskite phosphor achieved an RGL below 40% even at a high phosphor concentration of 10 wt%, appearing bluish in color (**Fig. S22**) on the original LED chip, indicating its poor color tunability and low PL intensity. Our NP-PP phosphor demonstrated a high RGL value because of its strong PL enhancement. When compared at the same phosphor concentration of 10 wt%, the RGL of the optimized NP-PP phosphor (matrix content of 3.5 wt%) exceeded 85%, which was approximately 2.2-fold that of the pure perovskite phosphor. These results confirm the excellent color tunability of the NP-PP phosphor owing to its strong PEO effect and high PL intensity.

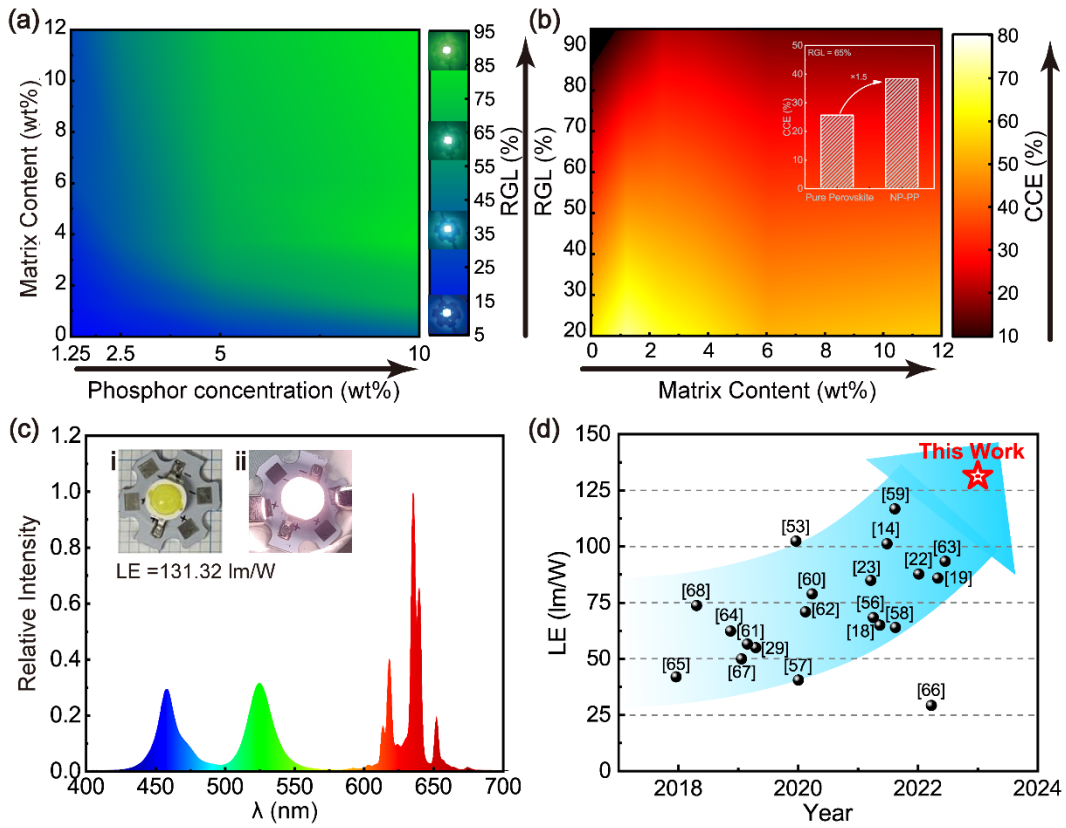

Fig. 7. Color conversion performance of NP-PP phosphor for LED devices. (a) RGL of NP-PP LEDs with different phosphor concentrations and matrix contents. (b) Relationship between RGL and CCE of NP-PP LEDs with different matrix contents. Inset: CCE comparison of pure perovskite and NP-PP when RGL = 65%. (c) Spectrum and PEO efficiency of white LED device using NP-PP phosphor as green converters. (i)-(ii) photograph of the white LED operated at 10 mA. (d) LE comparisons of white LEDs using halide perovskite as color converters.

Although a high PL intensity helps to achieve good color tunability, it is also

accompanied by a low color-conversion efficiency (CCE) introduced by conversion loss, especially the PL energy absorption loss mentioned above [55]. It is essential to simultaneously obtain high CCE and RGL values when comparing the PEO performance among different color converters [53]. Therefore, both the CCE and RGL values are provided in **Fig. 7b** for comparing NP-PP phosphor with different matrix contents. The CCE showed the same trend as the PLQY and PL intensity discussed above, which increased with an increase in the matrix content and then appeared as a roll-off. Additionally, the CCE value significantly dropped at high RGL values of over 60%. For example, the CCE of pure perovskite phosphor dropped to 14% when the RGL reached 80%. These results are consistent with previous reports and attributed to severe PL energy absorption loss at high phosphor concentrations [54]. However, our optimized NP-PP phosphor (matrix content of 3.5 wt%) maintained high CCE values ranging from 30 to 40% corresponding to high RGL values, which was 50% higher than that of the pure perovskite phosphor (when RGL = 65%). These results confirm that the NP-PP structure is beneficial to improve the PEO efficiency of the perovskite phosphor, simultaneously causing higher CCE and RGL values, compared to the pure perovskite phosphor, which are two key factors for the real application of color converters.

For comparison with reported studies, white LEDs combining green NP-PP phosphor and commercial red KSF ($K_2SiF_6:Mn^{4+}$) phosphor were prepared as

shown in **Fig. 7c**. Our NP-PP phosphor exhibited an ultrahigh LE of 131.32 lm/W according to the entrusted test recognized by the China National Accreditation Service (**Fig. S23**); the corresponding color coordinates are (0.3335, 0.2987) and the color gamut was 121% the value provided in National Television Standards Committee (NTSC) standards (**Fig. S24**). Notably, the LE of our NP-PP phosphor is higher than that in current reported white LEDs using green perovskite phosphor (**Fig. 7d**) [14, 18, 19, 22, 23, 29, 53, 56-68]. Such a high enhancement of NP-PP phosphor can be also confirmed by the referenced white LEDs using pure perovskite phosphor (**Fig. S25**). These results confirm the excellent PEO performance of NP-PP phosphor, which is caused by the well-designed NP-PP structure as discussed above. Besides, our NP-PP phosphor preserved the excellent working stability of the halide perovskite phosphor class (**Fig. S26**) [69, 70]. Slight (< 5%) PL attenuation was observed after being heated at 90 ℃ for 50 h. Consequently, our work provides essential insights into obtaining perovskite phosphors that have evolved from highly efficient materials (high PLQY) to highly efficient applications (high PEO) by utilizing the IRS effect in phosphor, significantly accelerating the application in optoelectronic applications.

3. Conclusions

In this study, we utilized the IRS effect to boost the PEO of $CsPbBr_3/Cs_4PbBr_6$ perovskite phosphor, which was realized by the NP-PP structure *in-situ* synthesized in the phosphor. A NMHS-LI reaction was developed

to prepare the NP-PP phosphor, key parameters, i.e., ultrasonic power and matrix content, were investigated to analyze the synthesis process. The optimized phosphor with a denser NP-PP structure has excellent dispersity and enhanced PL intensity, leading to the strong PEO (2.8-fold enhanced PL intensity) compared with the pure perovskite phosphor. FDTD simulation results revealed that the NP-PP structure can transform the PL energy absorption mode to the IRS mode, most of the scattering PL energy evades NP-PPs instead of propagating inside, and thus reducing the PL energy absorption loss. Finally, the optimized NP-PP phosphor was applied to white LEDs, high RGL and CCE values can be simultaneously obtained owing to the largely enhanced PL intensity extracting by the IRS effect, thereby achieving ultrahigh LE of 131.32 lm/W based on green perovskite phosphors. This study provides a general guide for efficient perovskite phosphors utilizing the nano-porous matrix to enable the IRS effect, which greatly accelerate the replacement of rare earth phosphor. Additionally, a detailed design of nanopore structures of the matrix-based perovskite phosphor is essential to further improve the PEO performance in future.

4. Experimental section

Materials: Cesium bromide (CsBr, 99.5%) and lead bromide ($PbBr_2$, 99%) were purchased from Shanghai Macklin Biochemical Co., Ltd. Ethyl acetate (EA, 99%) was purchased from Shanghai Aladdin Biochemical Technology Co., Ltd. N,N-dimethylformamide (DMF, 99.5%) and n-hexane (C6H14, 97%) were purchased

from DAMAO Chemical Reagent Factory. Aerogel (SiO_2) was purchased from Hengqiu Tech. Inc. Poly (dimethyl siloxane) (PDMS) was purchased from Dow Corning. Red K2SiF6:Mn4+ (KSF) phosphors were purchased from Shenzhen Looking Long Technology Co., Ltd. Blue LED devices were purchased from Foshan Nationstar Optoelectronics Company Ltd. All chemicals were used directly without any further purification.

Preparation of Cs-precursor: CsBr (6 mmol) was dissolved in deionized water (5 mL) and aerogel (x mg, x = 0, 20, 40, 60, 80, 100, equivalent to the matrix content of 0 wt%, 1.2 wt%, 2.3 wt%, 3.5 wt%, 4.6 wt% and 5.7 wt%, respectively) was dispersed in ethanol (5 mL), which was assisted by stirring or ultrasonication. The solution and dispersion liquids were then mixed and dried at 100 °C. The dried solids were finally ground into powders.

Synthesis of pure perovskite phosphor and NP-PP phosphor: First, for the synthesis of the pure perovskite phosphor, $PbBr_2$ (1 mmol) and CsBr (y mmol, y = 1, 2, 4, 6, 8, 10) were dissolved in DMF (10 mL); for the synthesis of NP-PP phosphor, $PbBr_2$ (1 mmol) and Cs-precursor were dissolved in DMF (10 mL). Second, the solution was placed in an ultrasonic crusher (BANDELIN, Electronic GmbH) for the NMHS-LI reaction (p W, 5 min, 50 s ON, and 10 s OFF; p = 0, 20, 30, 40, 60, 80), whose probe was inserted below half the depth of the liquid level. Third, the solution was transferred into a 20 mL centrifuge tube for centrifugation

(2000 rpm, 5 min). The supernatant was removed, and the precipitate was dissolved in EA (10 ml) and centrifuged (2000 rpm, 5 min) for purification. Next, the previous step was repeated, and the EA was replaced with n-hexane. Finally, the precipitate was dried and ground into powders.

Fabrication of pure perovskite and NP-PP films: The as-prepared pure perovskite phosphor or NP-PP phosphor (z mg, z = 25, 51, 105, 222, equivalent to the phosphor concentration of 1.25 wt%, 2.5 wt%, 5 wt% and 10 wt%, respectively) was uniformly mixed with polydimethylsiloxane (PDMS, 1.8 g) and a curing agent (0.2 g) by vacuum defoaming for 5 min. Then, a flat square die (depth and width of 1 mm and 4 mm, respectively) along with the mixture was dried at 90 °C for 30 min to obtain a piece of pure perovskite or NP-PP film. After curing, the film was removed from the die.

Fabrication of white LED devices: The as-prepared pure perovskite phosphor (0.059 g) or NP-PP phosphor (0.020 g) was first grounded for minutes and then uniformly mixed with commercial red KSF phosphor (0.115 g), PDMS (0.9 g), and curing agent (0.1 g) by vacuum defoaming for 5 min. The mixture was later injected into blue LED devices to finish the package. After curing at 60 ℃ for 2 h, white LED devices were obtained.

Characterization: The morphology of the sample was characterized using

scanning electron microscope (SEM, Zeiss, Merlin) and high-resolution transmission electron microscope (TEM, FEI, Talos F200X G2). The TEM slice sample was obtained using focused ion beam scanning electron microscope (FIB-SEM, FEI, Scios 2 HiVac). The phase and crystallography of the products were characterized using an X-ray diffractometer (XRD, D/max3A, Bruker) at a scanning rate of 10°/min in the 2θ range from 10 to 80° using Cu Kα radiation (λ = 1.5418 Å). The corresponding EDS elemental mappings were captured on a Bruker Nano GmbH Berlin instrument with a primary energy of 15 keV. The PL spectra of the phosphors were recorded using a fluorescence spectrophotometer (RF-6000, Shimadzu) with a Xe lamp as an excitation source, whose samples were packaged in PDMS. The UV–vis absorption spectra and haze spectra of the pure perovskite phosphor and NP-PP phosphor were recorded using a UV–vis spectrometer (Shimadzu) in the wavelength range of 300-800 nm at 1 nm intervals. Time-resolved fluorescence spectra were recorded using a steady-state fluorescence spectrometer (FLS1000, Edinburgh). The PLQYs of the samples (powder state before packaging) were measured using an absolute PLQY spectrometer at an excitation wavelength of 365 nm (K.K. C9920, Hamamatsu Photonics). The N_2 adsorption/desorption isotherms and pore size distributions of the aerogel were obtained using a gas adsorption analyzer (TriStar II 3flex, Mike). The contact angles of the aerogel were measured using a surface contact angle tester (OCA40 Micro; Data Physics). The optical performances of the white LEDs were measured by an integrating sphere system (Instrument Systems), and the

injection current was provided by a power source (Keithley). All reliability tests were conducted under laboratory conditions at a constant ambient temperature of 25 °C.

Acknowledgements

The authors acknowledge financial support from Science & Technology Program of Guangdong Province (2020B0101030008, 2020B121202003), Natural Science Foundation of Guangdong Province (2022A1515011059), China Postdoctoral Science Foundation (2020M680122, 2022M710697).

Appendix A. Supplementary information

Supplementary information associated with this article can be found in the online version.

References

[1] Q. Chen, J. Wu, X. Ou, B. Huang, J. Almutlaq, A.A. Zhumekenov, X. Guan, S. Han, L. Liang, Z. Yi, J. Li, X. Xie, Y. Wang, Y. Li, D. Fan, D.B.L. Teh, A.H. All, O.F. Mohammed, O.M. Bakr, T. Wu, M. Bettinelli, H. Yang, W. Huang, X. Liu, All-inorganic perovskite nanocrystal scintillators, Nature 561(7721) (2018) 88-93. https://doi.org/10.1038/s41586-018-0451-1.

[2] K. Lin, J. Xing, L.N. Quan, F.P.G. de Arquer, X. Gong, J. Lu, L. Xie, W. Zhao, D. Zhang, C. Yan, W. Li, X. Liu, Y. Lu, J. Kirman, E.H. Sargent, Q. Xiong, Z. Wei, Perovskite light-emitting diodes with external quantum efficiency exceeding 20 per cent, Nature 562(7726)

(2018) 245-248. https://doi.org/10.1038/s41586-018-0575-3.

[3] Y. Chen, Y. Lei, Y. Li, Y. Yu, J. Cai, M.-H. Chiu, R. Rao, Y. Gu, C. Wang, W. Choi, H. Hu, C. Wang, Y. Li, J. Song, J. Zhang, B. Qi, M. Lin, Z. Zhang, A.E. Islam, B. Maruyama, S. Dayeh, L.-J. Li, K. Yang, Y.-H. Lo, S. Xu, Strain engineering and epitaxial stabilization of halide perovskites, Nature 577(7789) (2020) 209-215. https://doi.org/10.1038/s41586-019-1868-x.

[4] C. Qin, A.S.D. Sandanayaka, C. Zhao, T. Matsushima, D. Zhang, T. Fujihara, C. Adachi, Stable room-temperature continuous-wave lasing in quasi-2D perovskite films, Nature 585(7823) (2020) 53-57. https://doi.org/10.1038/s41586-020-2621-1.

[5] C. Chen, S. Zheng, H. Song, Photon management to reduce energy loss in perovskite solar cells, Chemical Society Reviews 50(12) (2021) 7250-7329. https://doi.org/10.1039/d0cs01488e.

[6] X.-K. Liu, W. Xu, S. Bai, Y. Jin, J. Wang, R.H. Friend, F. Gao, Metal halide perovskites for light-emitting diodes, Nature Materials 20(1) (2021) 10-21. https://doi.org/10.1038/s41563-020-0784-7.

[7] S. Tan, T. Huang, I. Yavuz, R. Wang, T.W. Yoon, M. Xu, Q. Xing, K. Park, D.-K. Lee, C.-H. Chen, R. Zheng, T. Yoon, Y. Zhao, H.-C. Wang, D. Meng, J. Xue, Y.J. Song, X. Pan, N.-G. Park, J.-W. Lee, Y. Yang, Stability-limiting heterointerfaces of perovskite photovoltaics, Nature (2022). https://doi.org/10.1038/s41586-022-04604-5.

[8] L. Protesescu, S. Yakunin, M.I. Bodnarchuk, F. Krieg, R. Caputo, C.H. Hendon, R.X. Yang, A. Walsh, M.V. Kovalenko, Nanocrystals of Cesium Lead Halide Perovskites (CsPbX3, X = Cl, Br, and I): Novel Optoelectronic Materials Showing Bright Emission with Wide Color Gamut, Nano Letters 15(6) (2015) 3692-3696. https://doi.org/10.1021/nl5048779.

[9] D.D. Yang, X.M. Li, W.H. Zhou, S.L. Zhang, C.F. Meng, Y. Wu, Y. Wang, H.B. Zeng, CsPbBr3 Quantum Dots 2.0: Benzenesulfonic Acid Equivalent Ligand Awakens Complete Purification, Advanced Materials 31(30) (2019). https://doi.org/10.1002/adma.201900767.

[10] C.H. Lu, G.V. Biesold, Y.J. Liu, Z.T. Kang, Z.Q. Lin, Doping and ion substitution in colloidal metal halide perovskite nanocrystals, Chemical Society Reviews 49(14) (2020) 4953-5007. https://doi.org/10.1039/c9cs00790c.

[11] I. Moreels, Y. Justo, B. De Geyter, K. Haustraete, J.C. Martins, Z. Hens, Size-Tunable, Bright, and Stable PbS Quantum Dots: A Surface Chemistry Study, ACS Nano 5(3) (2011) 2004-2012. https://doi.org/10.1021/nn103050w.

[12] L.H. Qu, X.G. Peng, Control of photoluminescence properties of CdSe nanocrystals in growth, Journal of the American Chemical Society 124(9) (2002) 2049-2055. https://doi.org/10.1021/ja017002j.

[13] X.G. Wu, H. Ji, X. Yan, H. Zhong, Industry outlook of perovskite quantum dots for display applications, Nature Nanotechnology (2022). https://doi.org/10.1038/s41565-022-01163-8.

[14] K. Du, L. He, S. Song, J. Feng, Y. Li, M. Zhang, H. Li, C. Li, H. Zhang, In Situ Embedding Synthesis of Highly Stable CsPbBr3/CsPb2Br5@PbBr(OH) Nano/Microspheres through Water Assisted Strategy, Advanced Functional Materials 31(36) (2021). https://doi.org/10.1002/adfm.202103275.

[15] K.Y. Baek, W. Lee, J. Lee, J. Kim, H. Ahn, J.I. Kim, J. Kim, H. Lim, J. Shin, Y.J. Ko, H.D. Lee, R.H. Friend, T.W. Lee, J. Lee, K. Kang, T. Lee, Mechanochemistry-driven engineering of 0D/3D heterostructure for designing highly luminescent Cs-Pb-Br perovskites, Nat Commun 13(1) (2022) 4263. https://doi.org/10.1038/s41467-022-31924-x.

[16] H.W. Lian, Y. Li, K. Sharafudeen, W.R. Zhao, G.R. Krishnan, S.A. Zhang, J.R. Qiu, K. Huang, G. Han, Highly Thermotolerant Metal Halide Perovskite Solids, Advanced Materials 32(28) (2020). https://doi.org/10.1002/adma.202002495.

[17] DOE BTO Solid-State Lighting Program, 2022 DOE SSL R&D Opportunities, 2022. https://www.energy.gov/sites/default/files/2022-02/2022-ssl-rd-opportunities.pdf. (Accessed 2 February 2022).

[18] Y.Y. Duan, G.Z. Yin, D.Y. Wang, R.D. Costa, In Situ Ambient Preparation of Perovskite-

Poly(L-lactic acid) Phosphors for Highly Stable and Efficient Hybrid Light-Emitting Diodes, ACS Applied Materials & Interfaces 13(18) (2021) 21800-21809. https://doi.org/10.1021/acsami.1c04025.

[19] T.T. Xuan, S.Q. Guo, W.H. Bai, T.L. Zhou, L. Wang, R.J. Xie, Ultrastable and highly efficient green-emitting perovskite quantum dot composites for Mini-LED displays or backlights, Nano Energy 95 (2022). https://doi.org/10.1016/j.nanoen.2022.107003.

[20] J.S. Li, Y. Tang, Z.T. Li, J.X. Li, X.R. Ding, B.H. Yu, S.D. Yu, J.Z. Ou, H.C. Kuo, Toward 200 Lumens per Watt of Quantum-Dot White-Light-Emitting Diodes by Reducing Reabsorption Loss, ACS Nano 15(1) (2021) 550-562. https://doi.org/10.1021/acsnano.0c05735.

[21] A. Fakharuddin, M.K. Gangishetty, M. Abdi-Jalebi, S.H. Chin, A.B. Yusoff, D.N. Congreve, W. Tress, F. Deschler, M. Vasilopoulou, H.J. Bolink, Perovskite light-emitting diodes, Nature Electronics 5(4) (2022) 203-216. https://doi.org/10.1038/s41928-022-00745-7.

[22] J.J. Ren, A. Meijerink, X.P. Zhou, J.P. Wu, G.Y. Zhang, Y.H. Wang, In Situ Embedding Synthesis of CsPbBr3@Ce-MOF@SiO2 Nanocomposites for High Efficiency Light-Emitting Diodes: Suppressing Reabsorption Losses through the Waveguiding Effect, ACS Applied Materials & Interfaces 14(2) (2022) 3176-3188. https://doi.org/10.1021/acsami.1c20804.

[23] Q. Zhang, W. Zheng, Q. Wan, M. Liu, X. Feng, L. Kong, L. Li, Confined Synthesis of Stable and Uniform CsPbBr3 Nanocrystals with High Quantum Yield up to 90% by High Temperature Solid - State Reaction, Advanced Optical Materials 9(11) (2021). https://doi.org/10.1002/adom.202002130.

[24] J. Chen, S. Mukherjee, W. Li, H. Zeng, R.A. Fischer, Bespoke crystalline hybrids towards the next generation of white LEDs, Nature Reviews Materials (2022). https://doi.org/10.1038/s41578-022-00476-3.

[25] K.M. McCall, K. Sakhatskyi, E. Lehmann, B. Walfort, A.S. Losko, F. Montanarella, M.I. Bodnarchuk, F. Krieg, Y. Kelestemur, D. Mannes, Y. Shynkarenko, S. Yakunin, M.V.

Kovalenko, Fast Neutron Imaging with Semiconductor Nanocrystal Scintillators, ACS Nano 14(11) (2020) 14686-14697. https://doi.org/10.1021/acsnano.0c06381.

[26] L.N. Quan, R. Quintero-Bermudez, O. Voznyy, G. Walters, A. Jain, J.Z. Fan, X.L. Zheng, Z.Y. Yang, E.H. Sargent, Highly Emissive Green Perovskite Nanocrystals in a Solid State Crystalline Matrix, Advanced Materials 29(21) (2017) 6. https://doi.org/10.1002/adma.201605945.

[27] T. Jin, Z. Liu, J. Luo, J.-H. Yuan, H. Wang, Z. Xie, W. Pan, H. Wu, K.-H. Xue, L. Liu, Z. Hu, Z. Zheng, J. Tang, G. Niu, Self-wavelength shifting in two-dimensional perovskite for sensitive and fast gamma-ray detection, Nature Communications 14(1) (2023). https://doi.org/10.1038/s41467-023-38545-y.

[28] C.Y. Kong, C.H. Lin, C.H. Lin, T.Y. Li, S.W.H. Chen, C.L. Tsai, C.W. Sher, T.Z. Wu, P.T. Lee, X.Z. Xu, M.L. Zhang, C.H. Ho, J.H. He, H.C. Kuo, Highly Efficient and Stable White Light-Emitting Diodes Using Perovskite Quantum Dot Paper, Advanced Science 6(24) (2019). https://doi.org/10.1002/advs.201902230.

[29] T.T. Xuan, J.J. Huang, H. Liu, S.Q. Lou, L.Y. Cao, W.J. Gan, R.S. Liu, J. Wang, Super-Hydrophobic Cesium Lead Halide Perovskite Quantum Dot-Polymer Composites with High Stability and Luminescent Efficiency for Wide Color Gamut White Light-Emitting Diodes, Chemistry of Materials 31(3) (2019) 1042-1047. https://doi.org/10.1021/acs.chemmater.8b04596.

[30] J. Hao, Z. Dai, M. Guan, P. Dang, H. Wang, C. Yan, J. Lin, G. Li, Simultaneous enhancement of luminescence and stability of lead halide perovskites by a diatomite microcavity for light-emitting diodes, Chemical Engineering Journal 417 (2021). https://doi.org/10.1016/j.cej.2020.128056.

[31] W.Q. Yang, F. Gao, Y. Qiu, W.Z. Liu, H.Y. Xu, L.L. Yang, Y.C. Liu, CsPbBr3-Quantum-Dots/Polystyrene@Silica Hybrid Microsphere Structures with Significantly Improved Stability for White LEDs, Advanced Optical Materials 7(13) (2019).

https://doi.org/10.1002/adom.201900546.

[32] H.C. Wang, S.Y. Lin, A.C. Tang, B.P. Singh, H.C. Tong, C.Y. Chen, Y.C. Lee, T.L. Tsai, R.S. Liu, Mesoporous Silica Particles Integrated with All-Inorganic CsPbBr3 Perovskite Quantum-Dot Nanocomposites (MP-PQDs) with High Stability and Wide Color Gamut Used for Backlight Display, Angewandte Chemie International Edition 55(28) (2016) 7924-7929. https://doi.org/10.1002/anie.201603698.

[33] C. Sun, Y. Zhang, C. Ruan, C.Y. Yin, X.Y. Wang, Y.D. Wang, W.W. Yu, Efficient and Stable White LEDs with Silica-Coated Inorganic Perovskite Quantum Dots, Advanced Materials 28(45) (2016) 10088-10094. https://doi.org/10.1002/adma.201603081.

[34] J.W. Hou, P. Chen, A. Shukla, A. Krajnc, T.S. Wang, X.M. Li, R. Doasa, L.H.G. Tizei, B. Chan, D.N. Johnstone, R.J. Lin, T.U. Schulli, I. Martens, D. Appadoo, M.S. Ari, Z.L. Wang, T. Wei, S.C. Lo, M.Y. Lu, S.C. Li, E.B. Namdas, G. Mali, A.K. Cheetham, S.M. Collins, V. Chen, L.Z. Wang, T.D. Bennett, Liquid-phase sintering of lead halide perovskites and metal-organic framework glasses, Science 374(6567) (2021) 621-625. https://doi.org/10.1126/science.abf4460.

[35] Y. He, Y.J. Yoon, Y.W. Harn, G.V. Biesold-McGee, S. Liang, C.H. Lin, V.V. Tsukruk, N. Thadhani, Z.T. Kang, Z.Q. Lin, Unconventional route to dual-shelled organolead halide perovskite nanocrystals with controlled dimensions, surface chemistry, and stabilities, Science Advances 5(11) (2019). https://doi.org/10.1126/sciadv.aax4424.

[36] B. Mendewala, E.T. Vickers, K. Nikolaidou, A. DiBenedetto, W.G. Delmas, J.Z. Zhang, S. Ghosh, High Efficiency Luminescent Solar Concentrator based on Organo‐Metal Halide Perovskite Quantum Dots with Plasmon Enhancement, Advanced Optical Materials 9(20) (2021). https://doi.org/10.1002/adom.202100754.

[37] C.H. Bi, Z.W. Yao, X.J. Sun, X.C. Wei, J.X. Wang, J.J. Tian, Perovskite Quantum Dots with Ultralow Trap Density by Acid Etching-Driven Ligand Exchange for High Luminance and Stable Pure-Blue Light-Emitting Diodes, Advanced Materials 33(15) (2021).

https://doi.org/10.1002/adma.202006722.

[38] J.Z. Song, J.H. Li, L.M. Xu, J.H. Li, F.J. Zhang, B.N. Han, Q.S. Shan, H.B. Zeng, Room-Temperature Triple-Ligand Surface Engineering Synergistically Boosts Ink Stability, Recombination Dynamics, and Charge Injection toward EQE-11.6% Perovskite QLEDs, Advanced Materials 30(30) (2018). https://doi.org/10.1002/adma.201800764.

[39] Z. Li, C. Song, J. Li, G. Liang, L. Rao, S. Yu, X. Ding, Y. Tang, B. Yu, J. Ou, U. Lemmer, G. Gomard, Highly Efficient and Water‐Stable Lead Halide Perovskite Quantum Dots Using Superhydrophobic Aerogel Inorganic Matrix for White Light‐Emitting Diodes, Advanced Materials Technologies 5(2) (2020). https://doi.org/10.1002/admt.201900941.

[40] R. Cheng, Z.B. Liang, L. Zhu, H. Li, Y. Zhang, C.F. Wang, S. Chen, Fibrous Nanoreactors from Microfluidic Blow Spinning for Mass Production of Highly Stable Ligand-Free Perovskite Quantum Dots, Angew Chem Int Ed Engl 61(27) (2022) e202204371. https://doi.org/10.1002/anie.202204371.

[41] Z. Dong, D. Fernandez Rivas, S. Kuhn, Acoustophoretic focusing effects on particle synthesis and clogging in microreactors, Lab Chip 19(2) (2019) 316-327. https://doi.org/10.1039/c8lc00675j.

[42] M. Li, Z. Liu, W. Yao, C. Xu, Y. Yu, M. Yang, G. Chen, Ultrasonic cavitation-enabled microfluidic approach toward the continuous synthesis of cesium lead halide perovskite nanocrystals, Chinese Journal of Chemical Engineering 59 (2023) 32-41. https://doi.org/10.1016/j.cjche.2022.12.001.

[43] G.G. Li, Y. Tian, Y. Zhao, J. Lin, Recent progress in luminescence tuning of Ce3+ and Eu2+-activated phosphors for pc-WLEDs, Chemical Society Reviews 44(23) (2015) 8688-8713. https://doi.org/10.1039/c4cs00446a.

[44] W. Ding, H. Liu, S. Zhang, D. Qiu, X. Li, S. Wang, Transformation of Quasi‐2D Perovskite into 3D Perovskite Using Formamidine Acetate Additive for Efficient Blue Light‐Emitting

Diodes, Advanced Functional Materials 32(8) (2021). https://doi.org/10.1002/adfm.202105164.

[45] L. Zhao, J. Gao, Y.L. Lin, Y.W. Yeh, K.M. Lee, N. Yao, Y.L. Loo, B.P. Rand, Electrical Stress Influences the Efficiency of CH3NH3PbI3 Perovskite Light Emitting Devices, Advanced Materials 29(24) (2017). https://doi.org/10.1002/adma.201605317.

[46] Q.X. Zhong, M.H. Cao, H.C. Hu, D. Yang, M. Chen, P.L. Li, L.Z. Wu, Q. Zhang, One-Pot Synthesis of Highly Stable CsPbBr3@SiO2 Core-Shell Nanoparticles, ACS Nano 12(8) (2018) 8579-8587. https://doi.org/10.1021/acsnano.8b04209.

[47] L. Zhang, S. Lin, Dimensional tailoring of halide perovskite: A case study on Cs4PbBr6/CsPbBr3 hybrid with molecular halide perovskite, Solar Energy Materials and Solar Cells 204 (2020). https://doi.org/10.1016/j.solmat.2019.110237.

[48] H. Li, K. Wu, J. Lim, H.-J. Song, V.I. Klimov, Doctor-blade deposition of quantum dots onto standard window glass for low-loss large-area luminescent solar concentrators, Nature Energy 1(12) (2016). https://doi.org/10.1038/nenergy.2016.157.

[49] B. Mendewala, K. Nikolaidou, C. Hoffman, S. Sarang, J. Lu, B. Ilan, S. Ghosh, The potential of scalability in high efficiency hybrid perovskite thin film luminescent solar concentrators, Solar Energy 183 (2019) 392-397. https://doi.org/10.1016/j.solener.2019.03.042.

[50] Z.P. Hu, Z.Z. Liu, Y. Bian, S.Q. Li, X.S. Tang, J. Du, Z.G. Zang, M. Zhou, W. Hu, Y.X. Tian, Y.X. Leng, Enhanced Two-Photon-Pumped Emission from In Situ Synthesized Nonblinking CsPbBr3/SiO2 Nanocrystals with Excellent Stability, Advanced Optical Materials 6(3) (2018). https://doi.org/10.1002/adom.201700997.

[51] M.L. Zhang, Y. Li, K.M. Du, X. Gao, Y. Lu, D. Wen, S. Yao, J. Feng, H.J. Zhang, One-step conversion of CsPbBr3 into Cs4PbBr6/CsPbBr3@Ta2O5 core-shell microcrystals with enhanced stability and photoluminescence, Journal of Materials Chemistry C 9(4) (2021) 1228-1234. https://doi.org/10.1039/d0tc05039c.

[52] Y.G. Huang, E.L. Hsiang, M.Y. Deng, S.T. Wu, Mini-LED, Micro-LED and OLED displays:

present status and future perspectives, Light: Science & Applications 9(1) (2020). https://doi.org/10.1038/s41377-020-0341-9.

[53] Z.L. Zhang, L.L. Shen, H.L. Zhang, L. Ding, G.Z. Shao, X.J. Liang, W.D. Xiang, Novel red-emitting CsPb1-xTixI3 perovskite QDs@glasses with ambient stability for high efficiency white LEDs and plant growth LEDs, Chemical Engineering Journal 378 (2019). https://doi.org/10.1016/j.cej.2019.122125.

[54] M. He, W. Chunyun, J.Z. Li, J.W. Wu, S. Zhang, H.C. Kuo, L.Y. Shao, S.C. Zhao, J.Z. Zhang, F.Y. Kang, G.D. Wei, CsPbBr3-Cs4PbBr6 composite nanocrystals for highly efficient pure green light emission, Nanoscale 11(47) (2019) 22899-22906. https://doi.org/10.1039/c9nr07096f.

[55] Z.C. Li, L. Kong, S.Q. Huang, L. Li, Highly Luminescent and Ultrastable CsPbBr3 Perovskite Quantum Dots Incorporated into a Silica/Alumina Monolith, Angewandte Chemie International Edition 56(28) (2017) 8134-8138. https://doi.org/10.1002/anie.201703264.

[56] X.S. Tang, W.W. Chen, Z.Z. Liu, J. Du, Z.Q. Yao, Y. Huang, C. Chen, Z.Q. Yang, T.C. Shi, W. Hu, Z.G. Zang, Y. Chen, Y.X. Leng, Ultrathin, Core-Shell Structured SiO2 Coated Mn2+-Doped Perovskite Quantum Dots for Bright White Light-Emitting Diodes, Small 15(19) (2019). https://doi.org/10.1002/smll.201900484.

[57] H.L. Guan, S.Y. Zhao, H.X. Wang, D.D. Yan, M. Wang, Z.G. Zang, Room temperature synthesis of stable single silica-coated CsPbBr3 quantum dots combining tunable red emission of Ag-In-Zn-S for High-CRI white light-emitting diodes, Nano Energy 67 (2020). https://doi.org/10.1016/j.nanoen.2019.104279.

[58] Q.H. Mo, C. Chen, W.S. Cai, S.Y. Zhao, D.D. Yan, Z.G. Zang, Room Temperature Synthesis of Stable Zirconia-Coated CsPbBr3 Nanocrystals for White Light-Emitting Diodes and Visible Light Communication, Laser & Photonics Reviews 15(10) (2021). https://doi.org/10.1002/lpor.202100278.

[59] Y. Li, K.M. Du, M.L. Zhang, X. Gao, Y. Lu, S. Yao, C.Y. Li, J. Feng, H.J. Zhang, Tunable

795 ultra-uniform Cs4PbBr6 perovskites with efficient photoluminescence and excellent stability
796 for high-performance white light-emitting diodes, Journal of Materials Chemistry C 9(37)
797 (2021) 12811-12818. https://doi.org/10.1039/d1tc02210e.
798 [60] F. Zheng, B.B. Yang, P.Y. Cao, X.L. Qian, J. Zou, A novel bulk phosphor for white LDs:
799 CsPbBr3/Cs4PbBr6 composite quantum dots-embedded borosilicate glass with high PLQY
800 and excellent stability, Journal of Alloys and Compounds 818 (2020).
801 https://doi.org/10.1016/j.jallcom.2019.153307.
802 [61] H.G. Wu, S. Wang, F. Cao, J.P. Zhou, Q.Q. Wu, H.R. Wang, X.M. Li, L.Q. Yin, X.Y. Yang,
803 Ultrastable Inorganic Perovskite Nanocrystals Coated with a Thick Long-Chain Polymer for
804 Efficient White Light-Emitting Diodes, Chemistry of Materials 31(6) (2019) 1936-1940.
805 https://doi.org/10.1021/acs.chemmater.8b04634.
806 [62] Y.X. Liu, D. Li, L.L. Zhang, Y.J. Chen, C. Geng, S.S. Shi, Z.Z. Zhang, W.G. Bi, S. Xu,
807 Amine- and Acid-Free Synthesis of Stable CsPbBr3 Perovskite Nanocrystals, Chemistry of
808 Materials 32(5) (2020) 1904-1913. https://doi.org/10.1021/acs.chemmater.9b04558.
809 [63] Y. Zhang, G.S. Li, G.N. Hou, J.Q. Lin, M.S. Chen, S.H. Liu, H.C. Lin, J.F. Fang, C.B. Jing,
810 J.H. Chu, Multidentate ligand passivation enabled enhanced photoluminescence and stability
811 of CsPbBr3 nanocrystals for white light-emitting diodes, Chemical Engineering Journal 438
812 (2022). https://doi.org/10.1016/j.cej.2022.135270.
813 [64] Y.H. Song, S.Y. Park, J.S. Yoo, W.K. Park, H.S. Kim, S.H. Choi, S. Bin Kwon, B.K. Kang,
814 J.P. Kim, H.S. Jung, D.H. Yoon, W.S. Yang, Y.S. Seo, Efficient and stable green-emitting
815 CsPbBr3 perovskite nanocrystals in a microcapsule for light emitting diodes, Chemical
816 Engineering Journal 352 (2018) 957-963. https://doi.org/10.1016/j.cej.2018.05.153.
817 [65] S.J. Liu, M.L. He, X.X. Di, P.Z. Li, W.D. Xiang, X.J. Liang, CsPbX3 nanocrystals films
818 coated on YAG:Ce3+ PiG for warm white lighting source, Chemical Engineering Journal 330
819 (2017) 823-830. https://doi.org/10.1016/j.cej.2017.08.032.
820 [66] C. Zhao, Y.K. Li, W.G. Ye, X.F. Shen, Z.C. Wen, X.Y. Yuan, Y.G. Cao, C.Y. Ma, Ligand-

Free CsPbBr3 Perovskite Quantum Dots in Silica-Aerogel Composites with Enhanced Stability for w-LED and Display by Substituting Pb2+ with Pr3+ or Gd3+ Ions, Advanced Optical Materials 10(10) (2022). https://doi.org/10.1002/adom.202102200.

[67] H.Y. Liu, Y.S. Tan, M.H. Cao, H.C. Hu, L.Z. Wu, X.Y. Yu, L. Wang, B.Q. Sun, Q. Zhang, Fabricating CsPbX3-Based Type I and Type II Heterostructures by Tuning the Halide Composition of Janus CsPbX3/ZrO2 Nanocrystals, ACS Nano 13(5) (2019) 5366-5374. https://doi.org/10.1021/acsnano.9b00001.

[68] Y.M. Chen, Y. Zhou, Q. Zhao, J.Y. Zhang, J.P. Ma, T.T. Xuan, S.Q. Guo, Z.J. Yong, J. Wang, Y. Kuroiwa, C. Moriyoshi, H.T. Sun, Cs4PbBr6/CsPbBr3 Perovskite Composites with Near-Unity Luminescence Quantum Yield: Large-Scale Synthesis, Luminescence and Formation Mechanism, and White Light-Emitting Diode Application, ACS Applied Materials & Interfaces 10(18) (2018) 15905-15912. https://doi.org/10.1021/acsami.8b04556.

[69] Y.S. Tan, R.Y. Li, H. Xu, Y.S. Qin, T. Song, B.Q. Sun, Ultrastable and Reversible Fluorescent Perovskite Films Used for Flexible Instantaneous Display, Advanced Functional Materials 29(23) (2019). https://doi.org/10.1002/adfm.201900730.

[70] C. Fan, H. Liu, J. Zhou, X. Dai, H. He, Z. Ye, Ultrastable and highly efficient CsPbBr3 composites achieved by dual-matrix encapsulation for display devices, Infomat (2023). https://doi.org/10.1002/inf2.12417.